Influence of Region-dependent Error Growth on the Predictability of Tropical Cyclone Track and Intensity in High-resolution HWRF Ensembles

Jie Feng[1,2*], Falko Judt[3], Jing Zhang[4*]

[1]*Department of Atmospheric and Oceanic Sciences and Institute of Atmospheric Sciences, Fudan University, Shanghai, China*

[2]*Shanghai Qi Zhi Institute, Shanghai, China*

[3]*Mesoscale and Microscale Meteorology Laboratory, National Center for Atmospheric Research, Boulder, CO, USA*

[4]*Shanghai Typhoon Institute, China Meteorological Administration, Shanghai, China*

Corresponding author: Jie Feng (fengjiefj@fudan.edu.cn) ; Jing Zhang (zhangj@typhoon.org.cn)

Key Points:

- The most sensitive region of initial errors for TC track uncertainties is not always in the environment but maybe within a TC.
- Uncertainties in TC intensity are most sensitive to initial errors in the TC inner core.
- The source of TC intensity predictability for a few days is the predictable environment.

Abstract

Further extension of skillful prediction of tropical cyclones (TCs) relies on in-depth studies about the intrinsic predictability of TCs. In this study, convection-resolving ensemble forecasts based on the Hurricane Weather Research and Forecasting model were adopted with perturbed initial conditions to study the error growth and intrinsic predictability of TCs. The new aspect of our study is the focus on the sensitivity of TC track and intensity predictability to initial errors in different regions, including (1) the inner core and outer rainbands (0-350 km), (2) the near environment (350-1300 km), and (3) the far environment (1300-3500 km).

The results of TC track predictability show that the most sensitive region of initial errors for TC track forecasts is case-dependent. For the TC case with striking track forecast errors (e.g., Typhoon Chan-hom, 2020), the initial errors in the combined region of the TC inner core and outer rainbands produce the largest track uncertainties compared to those in the near and far environment. However, for the TC case with a highly predictable track (e.g., Typhoon Maysak, 2020), the most sensitive region of initial errors is the near environment at early lead times and the far environment later. By contrast, the most sensitive region for TC intensity is the inner core for both cases. The surface wind structure of TC inner core at larger scales (wavenumbers 0-2) can be predicted for more than 3.5 days, while the structure at smaller scales can only be predicted for a few hours.

Plain Language Summary

The prediction of tropical cyclones (TCs) has progressively improved in the past few decades. How long can we further extend skillful TC prediction? The answer to this question relies on in-depth studies about TC intrinsic predictability. In this study, the HWRF-based convection-resolving ensemble forecasts were adopted with perturbed initial conditions to study the error growth and intrinsic predictability of TCs. The new aspect of our study is the focus on the sensitivity of TC track and intensity predictability to initial errors in different regions. The main conclusions include: (1) the most sensitive region of initial errors for TC track uncertainties is case-dependent and not always in the environment. The initial errors in the combined region of TC inner core and outer rainbands may produce much larger track errors than those in the near and far environments for TCs with low track predictability. (2) For TC intensity, the most sensitive region consistently locates within the TC inner core. The large-scale components (wavenumber 0-2) of TC inherent vortex flow can be predicted for more than 3.5 days, which is primarily attributed to the predictability of the synoptic-scale environment. By contrast, the remaining components (wavenumber >2) are only predictable for a few hours.

1 Introduction

The prediction of tropical cyclones (TCs) remains challenging despite recent progress in theory, observing systems, numerical models, and data assimilation. The intensity of TCs is a crucial indicator of their disaster potential and is one of the most difficult metrics to predict as a result of the complex multi-scale interactions in TCs (e.g., Wang and Wu, 2004; Gopalakrishnan et al., 2011). As is well known, the errors in forecasting TC intensity have only decreased at a slow rate during the last few decades (Cangialosi and Franklin, 2014; DeMaria et al., 2014). By contrast, the errors in forecasting the tracks of TCs have significantly decreased by more than half within the same time period (Katz and Murphy, 2015). Despite this improvement in predicting TC tracks, there can still be remarkable errors in the prediction of TC tracks, especially those with curving, looping, or stalling paths (e.g., Wu et al., 2014; Torn et al., 2015; Feng et al., 2022). The increasing difficulties in continuously lowering TC track and intensity forecast errors prompt fundamental questions about their intrinsic predictability.

It is widely recognized that the track of a TC is primarily determined by the large-scale environmental steering flow (e.g., Emanuel et al., 2004; Wu et al., 2005) and generally defined as the regional and multi-layer mean of the wind fields (Holland, 1993). The steering flow represents weather systems that surround a TC, such as the monsoon trough, the subtropical ridge, and the mid-latitude trough (e.g., Chia and Ropelewski, 2002; Wu et al., 2005). From the perspective of predictability, many studies have shown that errors in the structures and positions of these synoptic-scale systems give rise to errors in TC tracks (e.g., Ito and Wu, 2013; Torn et al., 2018; Ashcroft et al., 2021; Hazelton et al., 2023). For example, Nystrom et al. (2018) found that the dominant source of track errors for Hurricane Joaquin (2015) arose from the environmental region >300 km from the TC center based on an ensemble-based sensitivity analysis. Other studies have shown that the errors associated with the internal processes in a TC may produce significant differences in the TC environments, which then feed back into errors in the track (e.g., Anwender et al., 2008; Harr et al., 2008; Torn et al., 2015). The sensitivity of track forecasts to initial condition errors in specific regions remains a topic of disagreement, and there has been limited investigation into how this sensitivity may vary on a case-by-case basis.

Predicting TC intensity is more challenging than predicting TC tracks as a result of the complex interactions of dynamic and thermodynamic processes at multiple spatiotemporal scales (e.g., Wang and Wu, 2004; Gopalakrishnan et al., 2011). Decades of research have shown that TC intensity are affected by the large-scale environment, such as the vertical wind shear (e.g., Black et al., 2002; Chen et al., 2006; Tang and Emanuel, 2012, Rios-Berrios and Torn, 2017), the temperature and salinity of the upper ocean (e.g., Emanuel et al., 2004), and air–sea interactions (Emanuel, 1986; Chen et al., 2007, 2013; Ma et al., 2017, 2018). In addition to these environmental factors, the effects of internal mesoscale processes on the TC intensity have also been highlighted, including the eyewall convection, adiabatic warming of the inner core, and secondary eyewall replacement (e.g., Shapiro and Willoughby, 1982; Rogers, 2010; Zhang and Chen, 2012; Qin et al., 2021, 2023). The intricate interplay between the internal and environmental structures of TCs and the modulation of their spiral rainbands and secondary circulation has been widely documented (e.g., Houze et al., 2006; Judt and Chen, 2010, Li and Wang, 2012). These complex interactions can make it challenging to predict changes in TC intensity, and the question about the regions in which the physical processes dominantly control the TC intensity remains at the center of their predictability.

The predictability of the TC intensity is often examined by analyzing the sensitivity of the predictions of TC intensity and structure to discrepancies in the initial conditions. Sipple and Zhang (2008, 2010) showed that the initial errors associated with moist convection, even those with negligible magnitudes, increase rapidly and contaminate other physical processes at larger scales through the upscaling error growth, which severely limits the predictability of the TC intensity. Van Sang et al. (2008) and Shin and Smith (2008) concluded that small initial random perturbations of moisture in the boundary layer can cause strong asymmetries in the TC vortex, resulting in a larger spread of intensity. In addition to the limitation of predictability due to TC inner core processes alone, some studies have shown that the predictability of the TC intensity decreases (i.e., becomes more sensitive to initial uncertainties) when vertical wind shear increases (Zhang and Tao, 2013; Tao and Zhang, 2015; Finocchio and Majumdar, 2017). Judt and Chen (2016) found that complex interactions among the vertical wind shear, the mean vortex, and internal convective processes jointly contribute to uncertainties in the TC intensity. Although the sensitivity of TC intensity forecasts to multiple factors has been intensively explored, the relative sensitivity of the TC intensity to the initial errors in different regions has not been addressed explicitly.

There have been a few studies quantifying the upper bound of the predictability of the TC intensity . Kieu and Moon (2016) reported that the sample-mean forecast errors of the TC intensity measured by the maximum sustained surface wind (MSW) speed approach a saturation value of about 8–10 m s^{-1} in an axisymmetrical model and real-time data statistics. With this threshold, they gave an upper limit for the predictability of the MSW of about three days. Hakim (2013) derived a similar predictability limit of about three days for the azimuthal wind using analog forecasts based on long-range simulation data for an idealized axisymmetrical model. Kieu and Rotunno (2022) found that the spectral kinetic error growth for azimuthal wavenumbers reaches saturation after ~ 9 hr as compared to ~ 18 hr for the radial direction in an idealized simulation of TC. Zhong et al. (2018) estimated a possible range of two and a half to seven days for the TC intensity predictability over the western North Pacific basin using a local dynamic analog method. Their results, however, relied on simplified tropical cyclone models or algorithms in an ideal framework without considering the effect of multi-scale physical processes on the change in TC intensity.

Judt et al. (2016) investigated the scale-dependent predictability limits of the inner core surface winds of TCs in the cloud-resolving Weather Research and Forecasting (WRF) model using Fourier decomposition. They found that the error growth and the predictability limits of the surface wind speed were scale-dependent: (1) the mean vortex and wavenumber-1 asymmetry were predictable for > 7 days; (2) the scales associated with rain bands (wave numbers 2–5) were predictable for a few days; and (3) convective scales (wave numbers >7) were only predcitablt for 6–12 hrs. However, because Judt et al (2016) used a stochastic perturbation method that mimics model error and continuously perturbed the model fields, they could not address the question of the intrinsic predictability of TCs—that is, the extent to which prediction is possible if an almost perfect procedure is used (e.g., Lorenz, 1969; Sun and Zhang, 2016; Selz, 2019). Furthermore, Judt et al. (2016) only used a single case, and therefore did not explore the case dependence of the predictability of TC track and intensity .

In response to the limitations mentioned above, the present study aims to investigate the intrinsic predictability of the TC track and intensity using convection-resolving ensemble forecasts with perturbed initial conditions based on the Hurricane Weather Research and

Forecasting (HWRF) model for two distinct cases. To assess the varying sensitivity of track and intensity forecasts to different regions of initial errors, we investigated the error growth and dynamics of such region-dependent errors. We investigated Typhoons (TCs occurred in the Western Pacific) Chan-hom and Maysak in 2020, two cases that turned out to have very distinct track predictabilities. A comparison of the results for these two TCs will help to clarify the case dependence of the TC predictability.

This paper is organized as follows. Section 2 describes the model setup. Section 3 provides a brief review of the two typhoons and introduces the experimental design. The results of the intrinsic predictability analysis are presented and discussed in Sections 4 (track) and 5 (intensity). Section 6 discusses the results of the combined effect of the initial and boundary uncertainties on the predictability of TCs. Finally, Section 7 presents our conclusions and discussion.

2 Model setup

The ensemble forecasts used in our predictability analyses were generated using the latest version of the regional high-resolution HWRF model (version 4.0a). The HWRF model has been widely used for both operational forecasts and research of tropical storms (e.g., Lu et al., 2017; Zhang et al., 2016; Zhang et al., 2018; Feng et al., 2019, 2021). The HWRF model is configured with triply nested domains, including an innermost convection-resolving grid at 2 km horizontal resolution (D03; Fig. 1, purple box) and an intermediate grid at 6 km resolution (D02; Fig. 1, red box), enclosed by the stationary outer domain at 18 km resolution (D01; Fig. 1, outermost domain). The inner two domains (D02 and D03) follow the vortex to ensure that the TC stays in the domain with the highest resolution. The three domains roughly cover an area of 77°×77° for D01 (288×576 grid points), 27°×27° for D02 (304×604 grid points), and 7°×8° for D03 (265×472 grid points), with 61 vertical levels up to 2 hPa.

Convective processes for the two outer domains with resolutions of 18 and 6 km were parameterized using the simplified Arakawa–Schubert cumulus scheme (Han and Pan, 2006), but were simulated explicitly for the innermost domain at 2 km grid spacing. The effect of moist physical processes was simulated using the Ferrier–Aligo microphysics scheme (Ferrier, 1994, 2005). Other model physics schemes included the modified surface layer (Kwon et al., 2010) and non-local planetary boundary layer (Hong and Pan, 1996) parameterization schemes, and the Eta Geophysical Fluid Dynamics Laboratory longwave and shortwave radiation schemes (Schwarzkopf and Fels, 1991; Lacis and Hansen, 1974).

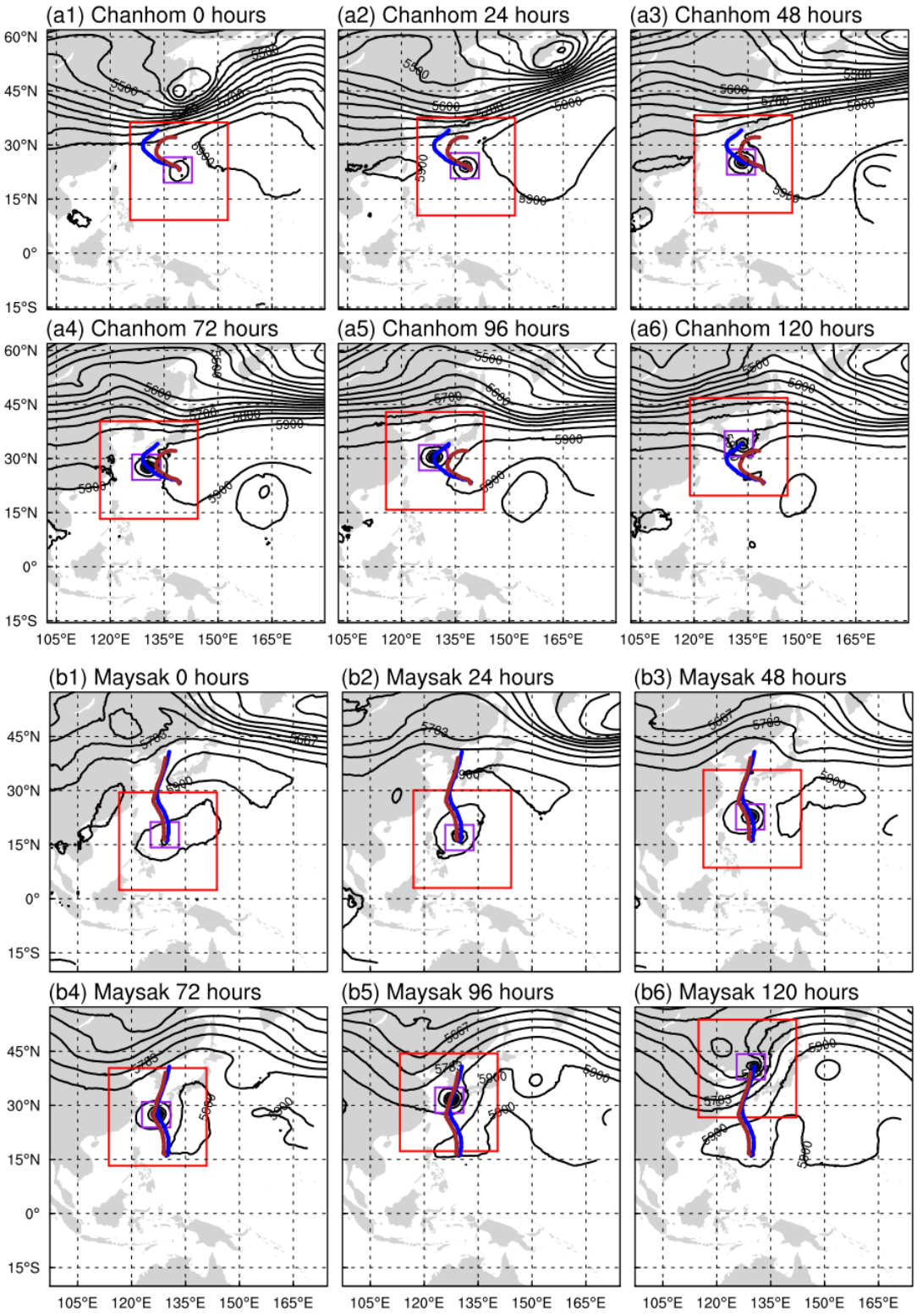

Figure 1. Evolution of the 500 hPa geopotential height in D01 for (a1–a6) Typhoon Chan-hom and (b1–b6) Typhoon Maysak during the control experiment from 0 to 120 h at intervals of 24 h

overlain by the tracks of the control (dark blue) and best-track observations (brown) within the same time period. The red and purple squares highlight areas D02 and D03.

3 Experimental setup

3.1 Review of the tropical cyclones

The two typhoons selected for this study were Typhoon Chan-hom, which occurred in early October 2020; and Typhoon Maysak, which lasted from the end of August to early September 2020. These two typhoons had remarkably different forecast uncertainty associated with their tracks (Fig. 1). The observed Typhoon Chan-hom intensified into a tropical storm (TS) at about 12 UTC on 5 October 2020 (i.e., the initial time of the forecasts in Fig. 1) and then moved northwestward and gradually turned toward the southern mainland of Japan. On 8 October, Typhoon Chan-hom turned sharply to the east while approaching peak intensity and then moved to the northeast off the eastern coast of Japan. The sharp turn to the east proved challenging for our five-day forecast experiment, and the simulated storm in the control run ended up turning too late and made landfall in Japan (*cf*. Fig. 1(a1–a6), blue and purple curves). By contrast, Typhoon Maysak's control forecast had smaller track forecast errors (<100 km) and featured much less uncertainty. This may have been associated with its stable northward motion from the East China Sea to landfall in South Korea.

The varying levels of forecast accuracy and associated uncertainties for the tracks of Typhoons Chan-hom and Maysak in both the control forecasts and observed outcomes suggest differing predictability for each. By comparing these two typhoons, we aim to gain a better understanding of the case-dependent sensitivity of initial errors in predicting the track and intensity of tropical cyclones. Notably, both Chan-hom and Maysak experienced prolonged lifetimes (lasting five to six days) over open waters without topographic influences. Moreover, they both maintained at least tropical storm intensity throughout their lifetime and eventually intensified into typhoons with maximum sustained winds exceeding 40 m s^{-1}.

3.2 Definition of the regions where perturbations will be introduced

As the main goal of our study was to investigate the intrinsic sensitivity of the TC track and intensity to region-dependent initial uncertainties, we used the three nested domains to roughly divide the structure and characteristics of TCs into three regions (Fig. 1 and Table 1). The innermost domain (i.e., D03) covers the TC inner core[1] and the outer spiral rainbands within about 350 km of the TC center almost five to six times the radius of the maximum wind. The region referred to in Table 1 as "part of D03" is also defined to investigate the role of the TC inner core (0–250 km) and the outer rainbands (250–350 km). The region between the innermost and intermediate domains (i.e., D02 and D03) from about 350 to 1300 km roughly corresponds to the environment adjacent to the TC vortex (defined as the near environment). The region between the intermediate and outer domains (i.e., D02 and D01) from 1300 to 3500 km roughly overlies the synoptic-scale weather systems at a long distance from the TC center (defined as the far environment).

[1] The inner core region of a strong TC generally includes the eye, eyewall, and the principle rain bands within about three times the radius of the maximum wind (Houze, 2010).

Table 1. Definitions of the regions in a tropical cyclone and their ranges and characteristics.

Region	Range (km)	Characteristics
D03	0–350	Inner core and outer rainbands
D03 to D02	350–1300	Near environment
D02 to D01	1300–3500	Far environment
Part of D03	0–250	Inner core
	250–350	Outer rainbands

3.3 Experimental design

Fig. 2 shows a flow diagram of the experiment. The first step is to generate the initial control and perturbed ensemble conditions ($N = 20$) valid at time t_0 for the three nested domains in the HWRF model. The initial conditions are 6-hr HWRF forecasts from time t_{-1} to t_0 initialized with the downscaled fields of the control analysis of the Global Forecast System (GFS, 0.25° resolution) and the perturbed analyses of the Global Ensemble Forecast System (GEFS, 0.5° resolution; Zhou et al., 2022) from the National Centers for Environment Prediction. The GFS forecasts provide the lateral boundary conditions for the 6-h HWRF control (red dashed arrow) and ensemble (black dashed arrow) forecasts, respectively. We use the 6-h short-term HWRF forecasts as the initial conditions instead of the downscaled GFS/GEFS fields to start the simulations with more realistic dynamically evolved and spatially coherent initial ensemble perturbations.

Once the initial control and ensemble conditions for the HWRF model are created, the second step is the design of numerical experiments to address the impact of the region-dependent initial errors on the TC predictability. The HWRF model adopts two-way communication for multiple nested domains in which the time- and space-interpolated values of the parent domain are specified on the nest boundaries while the inner domain is advanced (Moeng et al., 2007). The interior values of the nest domain are then transferred to the parent domain, overwriting the parent domain solution in the overlapped region. Perturbing the control analyses in D01, D02, and D03, therefore, introduces the initial errors associated with the far environment (but not the near environment nor the inner core and outer rainbands), the near environment (but not the far environment nor the inner core and outer rainbands), and the inner core and outer rainbands, respectively (Table 1).

Based on this concept, we defined the numerical experiments as follows (see Table 2). The baseline experiment (the Ctrl experiment) is the control analyses and forecasts (red solid arrow in Fig. 2). Experiment PertD01 uses the perturbed initial ensemble for D01, but the initial conditions for D02 and D03 are the same as in the Ctrl experiment. Similarly, experiments PertD02 and PertD03 simply perturb the initial conditions for D02 and D03, respectively. To determine the individual effects of uncertainties in the inner core and outer rainbands of the TC, experiments PertD03-Vor and PertD03-Rainb are carried out with the initial perturbations superposed on a smaller region than in PertD03—that is, the inner core and outer rainband

regions, respectively. These experiments (PertD01, PertD02, PertD03, PertD03-Vor, and PertD03-Rainb) use the same lateral boundaries as the Ctrl experiment to display the effects related to the initial error. Experiment PertAll retains all the perturbations in the initial ensemble of the three nested domains and the lateral boundaries.

The third step is to integrate the initial control and ensemble conditions from t_0 for all experiments for five days using the HWRF model with the output at intervals of 6 h. The initial time t_0 is the point at which the two typhoons reached TS intensity of nearly 18 m s^{-1}, i.e., 1200 UTC on 5 October 2020 for Typhoon Chan-hom and 0000 UTC on 29 August 2020 for Typhoon Maysak.

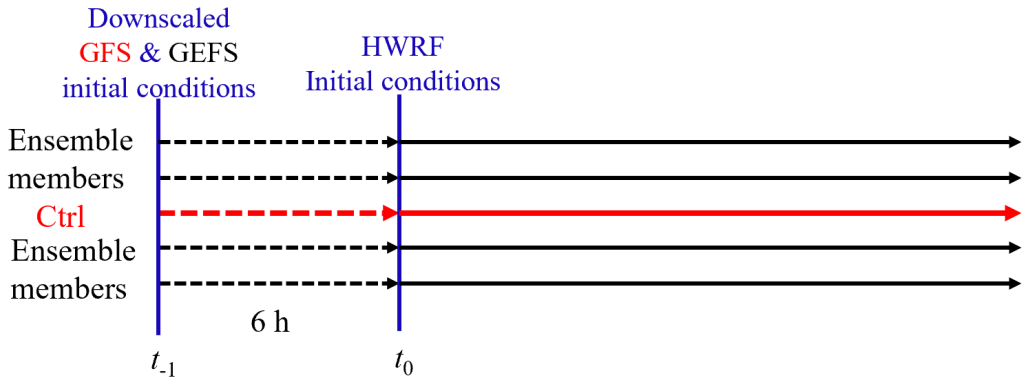

Figure 2. Schematic diagram of the experimental flow. GFS, Global Forecast System; GEFS, Global Ensemble Forecast System.

Table 2. Descriptions of the control (Ctrl) and ensemble forecast experiments.

	Ctrl	PertD01	PertD02	PertD03	PertD03-Vor	PertD03-Rainb	PertAll
D01 perturbed	No	Yes	No	No	No	No	Yes
D02 perturbed	No	No	Yes	No	No	No	Yes
D03 perturbed	No	No	No	Yes	Yes, vortex (0–250 km)	Yes, outer rainbands (250–350 km)	Yes
Boundary perturbed	No	No	No	No	No	No	Yes

4 Intrinsic predictability of the track of tropical cyclones

4.1 Track uncertainty

Fig. 3 shows the five-day ensemble track forecasts (green curves) for the two typhoons for experiments PertD01 (Fig. 3a1, b1), PertD02 (Fig. 3a2, b2), PertD03 (Fig. 3a3, b3), and PertD03-Vor (Fig. 3a4, b4) overlain with the TC tracks from the Ctrl experiment and the observations (blue and brown curves, respectively). Note that the ensemble track forecasts are compared with the Ctrl experiment rather than the observations in all subsequent analyses. As pointed out in Fig. 1, the Ctrl track errors of Typhoon Chan-hom when verified against the observations are significantly larger than those of Typhoon Maysak, which is consistent with the much larger spread of the ensemble track of Typhoon Chan-hom than that of Typhoon Maysak. This probably indicates the different intrinsic predictabilities of the two typhoons—that is, the track of Typhoon Maysak is inherently more predictable than that of Typhoon Chan-hom. The ensemble track spread exhibits striking variations among the experiments for each typhoon, indicating their contrasting sensitivities to the initial uncertainty regions.

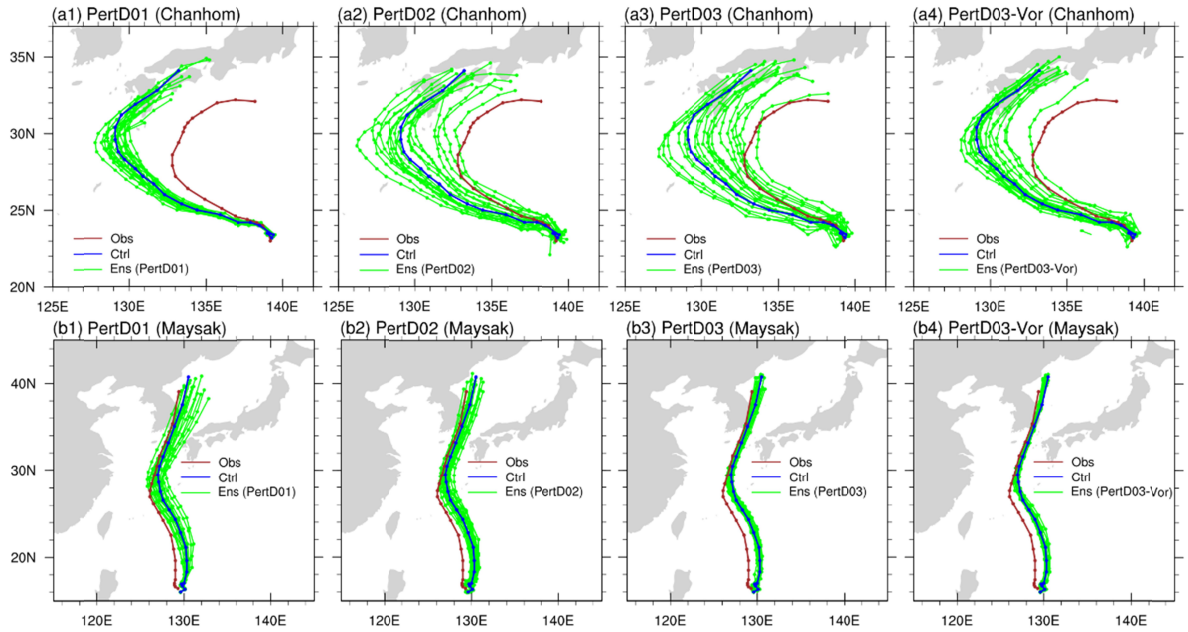

Figure 3. Five-day tracks in the Ctrl forecast (dark blue), observations (brown), and the ensemble forecasts (green) of (a1) PertD01, (a2) PertD02, (a3) PertD03, and (a4) PertD03-Vor for Typhoon Chan-hom and (b1) PertD01, (b2) PertD02, (b3) PertD03, and (b4) PertD03-Vor for Typhoon Maysak.

Fig. 4 further quantifies the ensemble track errors verified against the Ctrl forecast averaged over all ensemble members for Typhoons Chan-hom and Maysak. For Typhoon Chan-hom (Fig. 4a), PertD03 with initial errors in D03 shows the largest track errors at all lead times, followed by PertD02 and PertD01 with initial errors in the near and far environments, respectively. Noticeably, the comparison of PertD03 with PertD03-Vor and PertD03-Rainb shows that the mean TC track error is significantly reduced when the uncertainties in the outer rainband or the inner core region of the TC are removed. This interesting result may indicate that the high sensitivity of the TC track to initial errors in D03 is contributed to a large degree by the strong interaction of errors in the inner core and the outer rainbands (or the environment

interface in other words) of the TC (Houze, et al., 2006; Li and Wang, 2012) (see more details in Fig. 6).

By contrast, despite the smaller track errors overall, Typhoon Maysak shows qualitatively different results from Typhoon Chan-hom (*cf*. Fig. 4a and 4b), suggesting that the initial errors in the TC environment induce the largest track forecast errors. The most sensitive region is the near environment (i.e., PertD02) during the first 2.5 days, followed by the far environment (i.e., PertD01) for longer lead times. The comparison between Typhoons Chan-hom and Maysak suggests that the track errors for a TC with a low track predictability may be most sensitive to the initial uncertainties in the combined region of the inner core and outer rainband. By contrast, the track errors in a highly predictable TC may be most sensitive to the near environment in the earlier stages and then the outer environment for long-range predictions. The high track predictability is possibly associated with the weak interactions between the inner core and the outer rainband and environment (see Fig. 7 for more details).

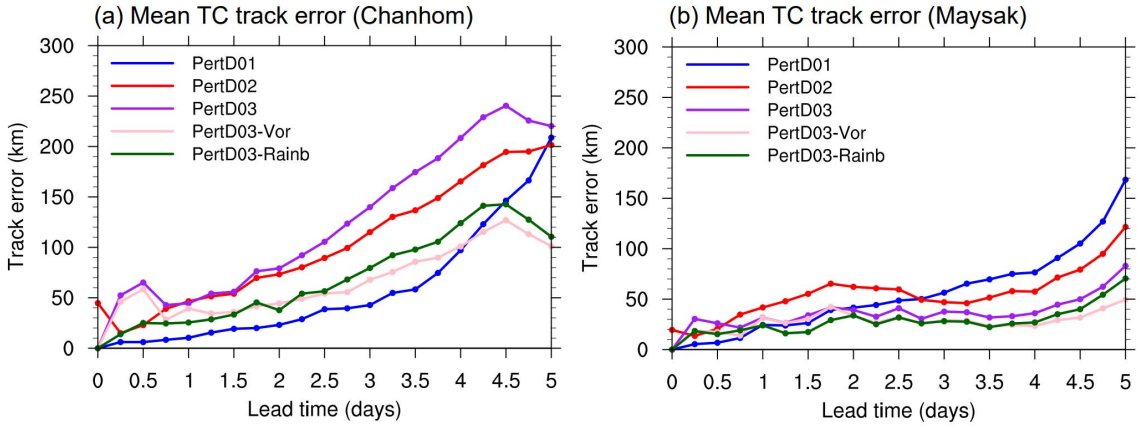

Figure 4. Track errors of the ensemble forecasts against the Ctrl forecast averaged over all ensemble members in PertD01 (dark blue), PertD02 (red), PertD03 (purple), PertD03-Vor (pink), and PertD03-Rainb (dark green) for Typhoons (a) Chan-hom and (b) Maysak.

4.2 Growth of region-dependent initial errors

To explore how region-specific initial errors lead to diverse outcomes in the predictability of TC tracks, we examined the ensemble-averaged error growth of the 500-hPa geopotential height (GH) and temperature (T) fields for different experiments. Fig. 5 shows the ensemble-averaged initial errors in the 500-hPa GH for D01 of PertD01, D02 of PertD02, and D03 of PertD03. The ensemble-averaged initial error of the 500-hPa T for D03 of PertD03-Vor is shown in Figs. 5a4 and 5b4 because the initial ensemble perturbations between the 250 and 350 km range in PertD03-Vor are removed for the state variables (the zonal and meridional winds, temperature, specific humidity, and sea-level pressure). Fig. 5 shows that the major initial errors in D02 and D03 for both Typhoons Chan-hom and Maysak are located near the TC eyewall (50–70 km from the typhoon center) (Fig. 5a2–5a4, 5b2–5b4). Another region of higher error magnitude is located near the trough region in the north of the TC environment (Fig. 5a1 and 5b1). This indicates the validity of the initial ensemble perturbations that capture the dynamic instabilities of a TC.

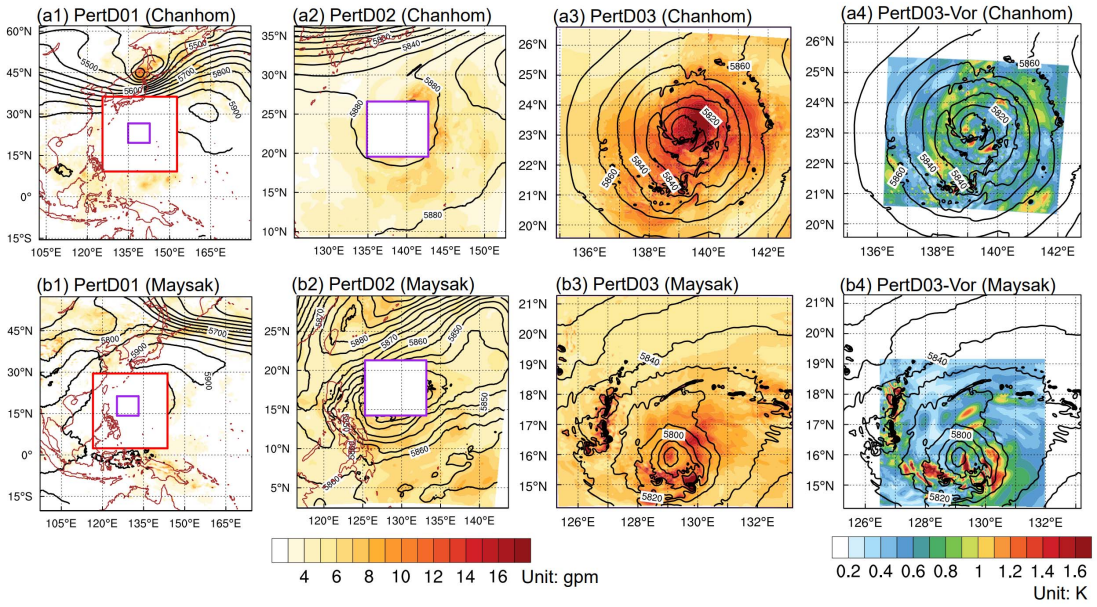

Figure 5. Ensemble-averaged initial error amplitudes of the 500-hPa geopotential height in (a1) D01 of PertD01, (a2) D02 of PertD02, and (a3) D03 of PertD03, and the 500-hPa temperature in (a4) D03 of PertD03-Vor for Typhoon Chan-hom. (b1)-(b4) are same as (a1)-(a4) but for Typhoon Maysak.

In addition to the initial error fields, the ensemble-averaged error growth of the 500 hPa GH (shaded) and T (contours) in D02 for different experiments is shown in Fig. 6 for Typhoon Chan-hom and in Fig. 7 for Typhoon Maysak. Domain D03 is highlighted (purple squares) for reference. Figs. 6a1 and 6b1 show that, even with initial errors in just the environment (i.e., PertD01 and PertD02), the errors in the TC inner core (D03) grow rapidly and display a comparable amplitude to those in the near environment within 12 h. This can be explained by the more intense error growth of mesoscale convective instabilities in the TC inner core than the error growth of baroclinic instabilities in the TC environment (Lorenz, 1996; Durran and Gingrich, 2014; Sun and Zhang, 2016). PertD03 and PertD03-Vor, with initially perturbed D03 present larger errors than PertD01 and PertD02 at 12 h, not only in domain D03 but also in domain D02 (*cf.* Figs. 6c1, 6d1 and Figs. 6a1, 6b1). This implies that initial errors in the TC inner core may spread out and lead to forecast uncertainties in the environment of the TC, probably through their intense interactions with the outer rainbands.

The error growth in the TC environment induced by such interactions and the upscale progression of error growth have a faster rate than the error growth of the environment *per se* in the first 24 h (*cf.* Fig. 6b2 and 6c2). After this transient period (about 24 h) of upscale error propagation from the fine-scale TC inner core to the synoptic-scale environment, the initial errors in the TC environment start to grow and dominate the expansion of forecast uncertainties in this region. This explains the larger forecast errors in the environment for PertD02 than for PertD03-Vor from 24 to 96 h (*cf.* Fig. 5b2–b4 and Fig. 5d2–d4). Experiment PertD03 shows the largest forecast errors in D02 relative to the other experiments for all lead times, especially for the TC environment. This further suggests the possibility that the particularly strong interaction

between the errors in the inner core and outer rainbands in PertD03 may rapidly produce errors in the environment of Typhoon Chan-hom. PertD01 presents the smallest overall forecast errors in D02 throughout all the experiments, which possibly indicates the weak sensitivity of Typhoon Chan-hom's track to the distant environment beyond about 1300 km. A clearer mechanism for the different sensitivity behavior of the predictability of TC tracks is warranted in future studies.

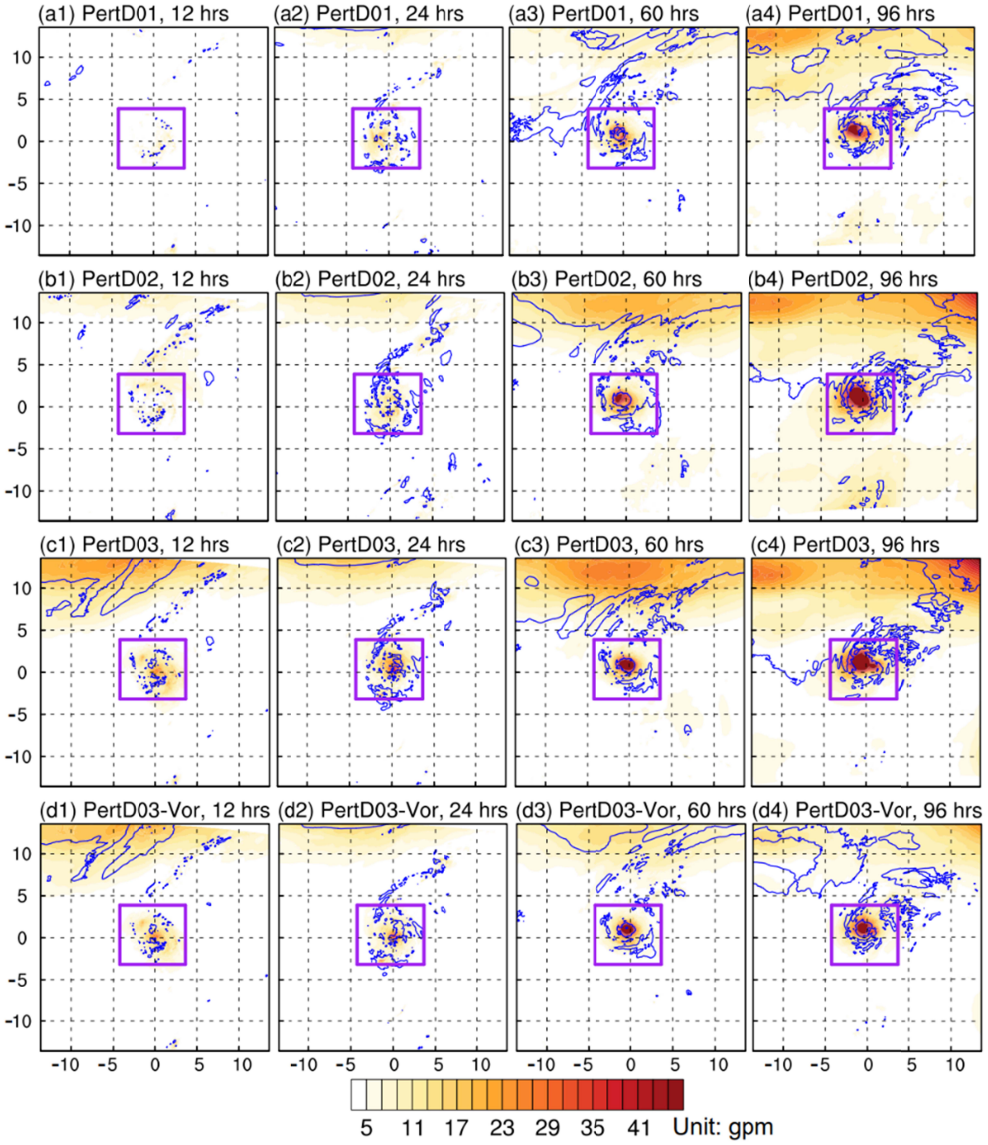

Figure 6. Ensemble-averaged absolute forecast errors of the 500-hPa GH (shading) and T (contours) for Typhoon Chan-hom in D02 of (a) PertD01, (b) PertD02, (c) PertD03, and (d) PertD03-Vor at (a1, b1, c1, d1) 12, (a2, b2, c2, d2) 24, (a3, b3, c3, d3) 60, and (a4, b4, c4, d4) 96 h. Temperature contours are 1, 5, and 9 K. Purple squares show domain D03.

Fig. 7 is the same as Fig. 6 but for Typhoon Maysak. It is consistent with Fig. 6 in that the errors in the TC inner core due to the strong convective instabilities grow much faster than those in the environment. However, in contrast with Typhoon Chan-hom, the forecast errors in

the near environment of Typhoon Maysak are slightly larger in PertD02 and PertD01 than in PertD03 and PertD03-Vor within the first 24 h (not shown), probably indicating a much weaker interaction between the inner and outer TC structures relative to Typhoon Chan-hom. Consequently, the growth of the initial errors in the TC environment plays a more important role in contributing to its larger forecast errors beyond 24 h compared with the initial errors in the inner core and outer rainbands of the TC (*cf.* PertD01, PertD02 and PertD03, PertD03-Vor in Fig. 7).

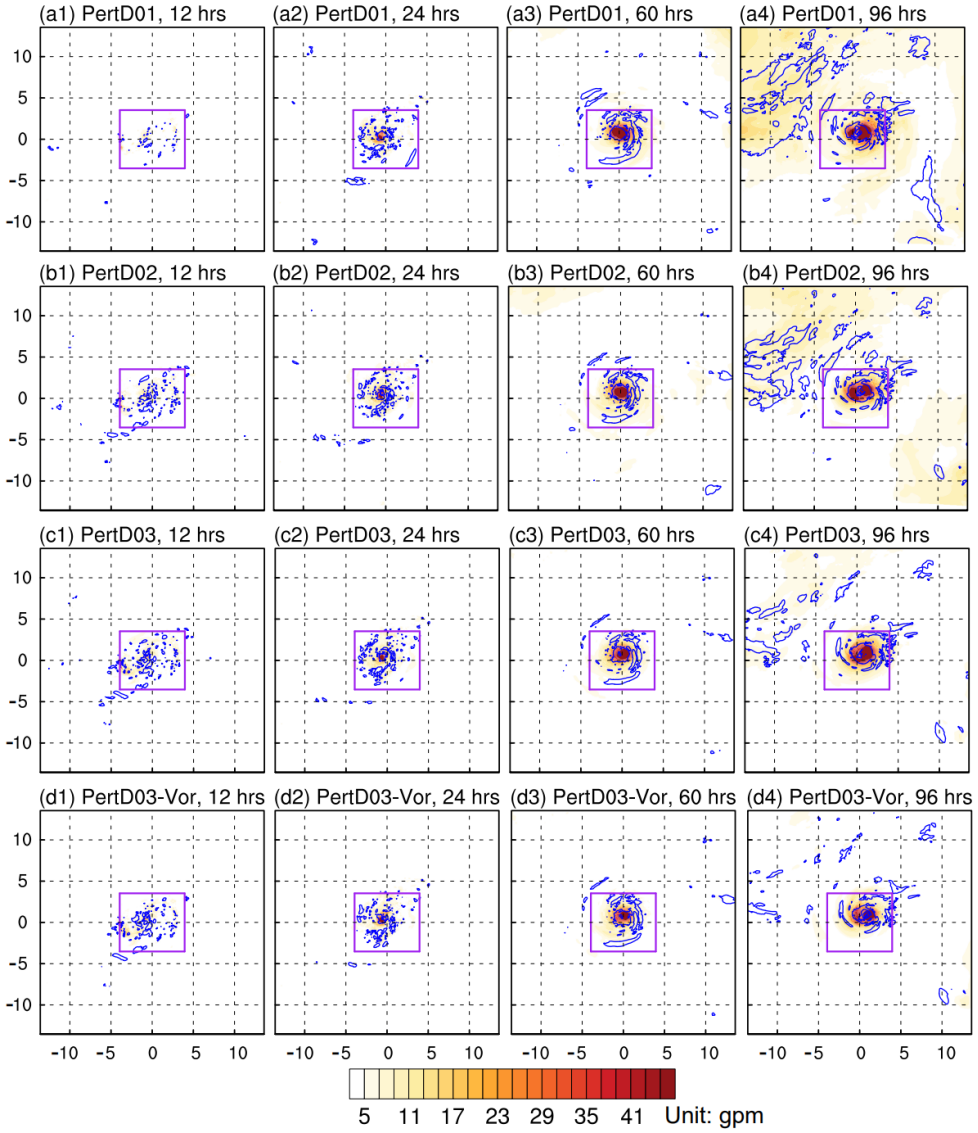

Figure 7. Same as Fig. 6 but for Typhoon Maysak.

5 Intrinsic predictability of the TC intensity

5.1 Intensity uncertainty

This section focuses on the forecast uncertainty for the TC intensity and the relevant error growth dynamics. The TC intensity is generally measured by two metrics: the minimum sea-

level pressure (MSLP) and the MSW. Fig. 8 shows the evolution of the MSLP and MSW in the ensemble and Ctrl forecasts and observations for Typhoon Chan-hom. The Ctrl forecast errors compared with the observations averaged over all lead times for Typhoon Chan-hom are about 10 hPa for the MSLP and 6 m s^{-1} for the MSW, which are about half of those for Typhoon Maysak (not shown). The ensemble intensity spread of Typhoon Chan-hom is also smaller overall than that of Typhoon Maysak (not shown). The difference in the intensity spread of Typhoons Chan-hom and Maysak implies that they have distinct intensity predictability. Similar to the forecasts of the TC ensemble tracks, the ensemble intensities also show different spreads in experiments PertD01, PertD02, PertD03, and PertD03-Vor for each typhoon (see more details below).

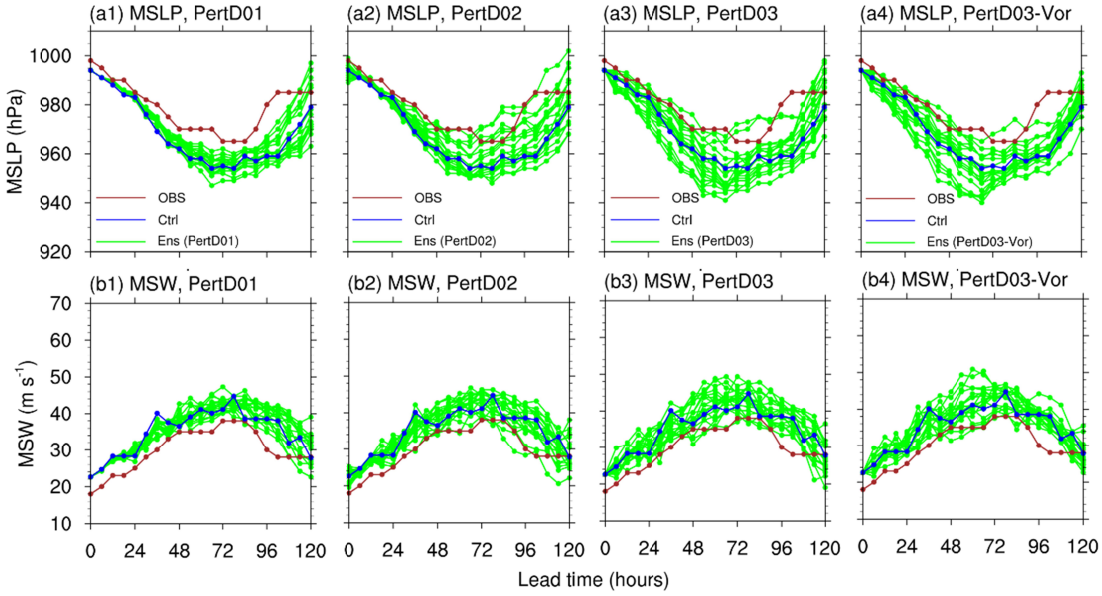

Figure 8. Five-day minimum (a) sea-level pressure (MSLP) and (b) MSW in the Ctrl forecast (dark blue), observations (brown), and ensemble forecasts (green) of (a1, b1) PertD01, (a2, b2) PertD02, (a3, b3) PertD03, and (a4, b4) PertD03-Vor for Typhoon Chan-hom.

The ensemble-averaged typhoon intensity forecast errors for experiments PertD01, PertD02, PertD03, and PertD03-Vor in Fig. 8 are calculated and shown in Fig. 9. For both typhoons, PertD03 (purple) shows larger errors in intensity than PertD01 (blue) and PertD02 (red) in terms of both the MSLP and MSW, especially within the first 2.5 days. The forecast errors in the intensity of PertD03 remain almost unchanged within the first 2.5 days, even with the removal of the initial uncertainties in the outer rainband region (*cf.* PertD03 and PertD03-Vor). These results confirm that the TC intensity is more sensitive to the inner-core structures within a 250 km radius than to the outer rainbands and environment of the TC. PertD02 (red) produces larger uncertainties in the TC intensity than PertD01 (dark blue), which indicates that the predictability of the TC intensity is more sensitive to initial errors in the near environment than in the far environment.

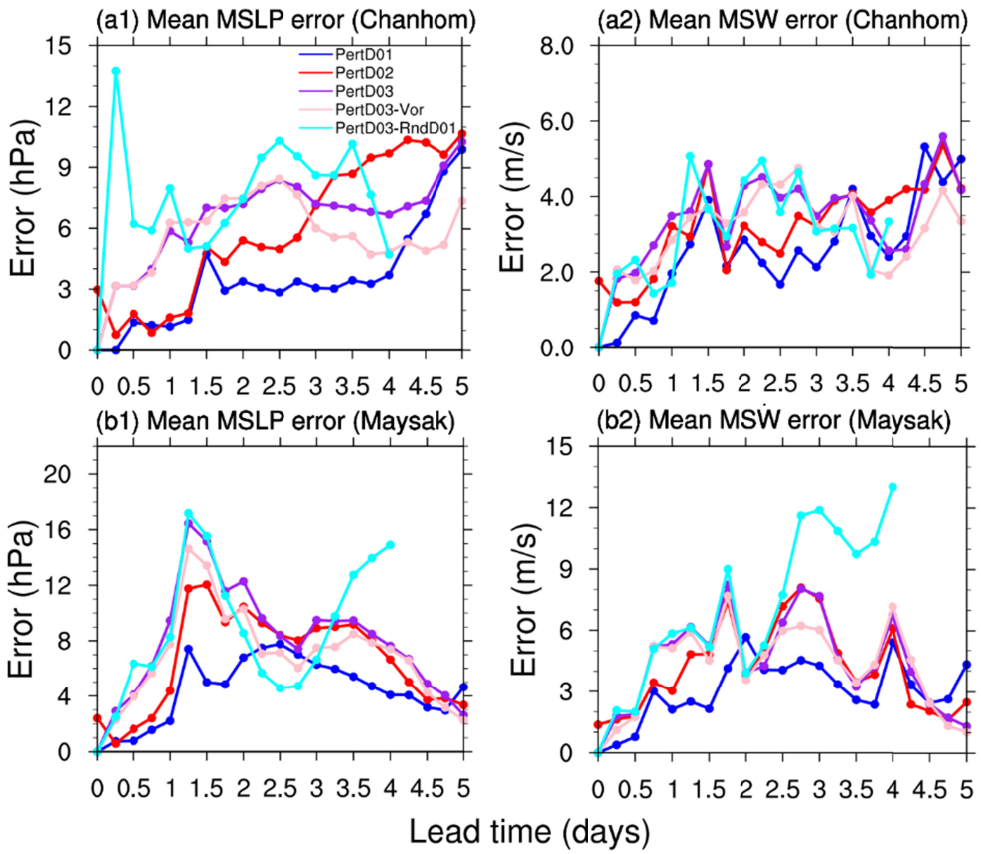

Figure 9. Intensity errors of the ensemble forecasts against the Ctrl forecast averaged over all ensemble members in PertD01 (dark blue), PertD02 (red), PertD03 (purple), PertD03-Vor (pink), and PertD03-RndD01 (cyan) in terms of the (a1, b1) MSLP and (a2, b2) MSW for (a) Typhoon Chan-hom and (b) Typhoon Maysak.

5.2 Scale-dependent error growth

Previous studies have shown that the TC intensity evolution is closely related to both the symmetrical and asymmetrical structures of the inner core (Moller and Montgomery, 2000; Nolan et al., 2007; Yang et al., 2007; Persing et al., 2013). To determine how the initial errors inherent in the TC influence the predictability of intensity, we used a Fourier decomposition algorithm to decompose the azimuthal structures of the 10-m wind amplitude field within a 300-km radius of the TC center, as in Judt et al. (2016). The original 10-m wind amplitude field within the 300-km radius can be decomposed into the mean state (i.e., wave number 0) and 180 wave component fields (Fig. 10). Following the classification of Judt et al. (2016), wave number 0 represents the mean vortex and wave number 1 is the vortex-scale asymmetry. The structure of wave numbers 2–5 resembles the TC rain bands and the remaining scales ≥6 are associated with smaller mesoscale and convective features in the TC circulation.

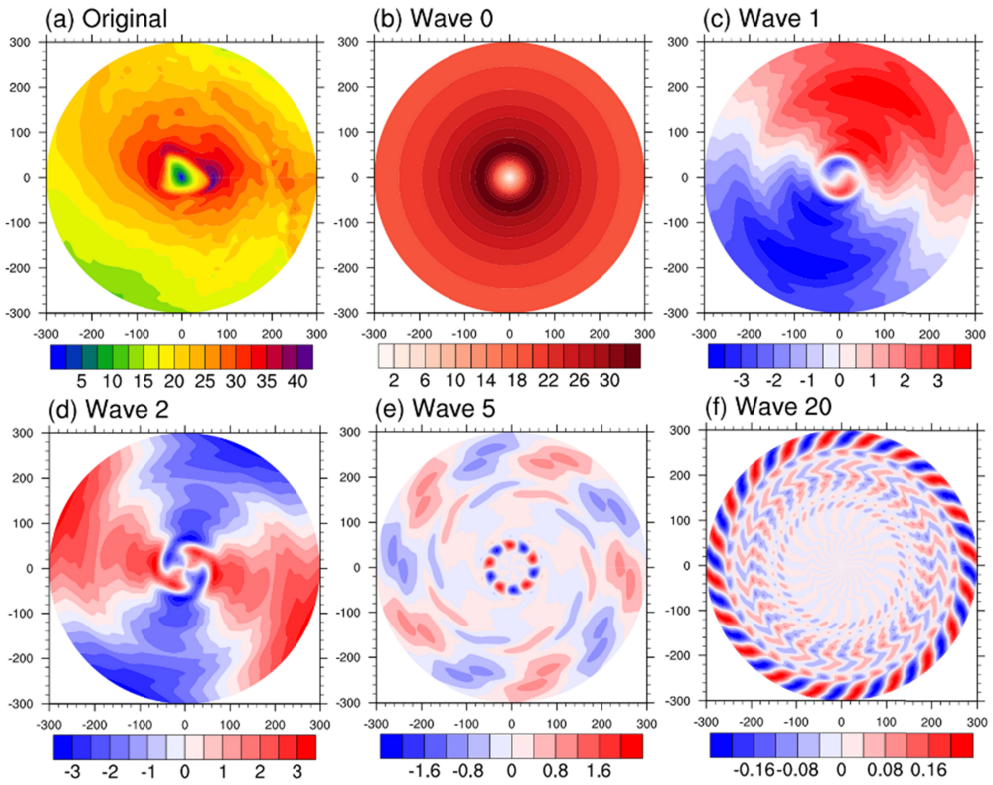

Figure 10. (a) 10-m wind speed (m s^{-1}) in a 300-km radius from the TC center in the 2.25-day Ctrl forecast of Typhoon Chan-hom and its azimuthally decomposed components at wave numbers (b) 0, (c) 1, (d) 2, (e) 5, and (f) 20.

Fig. 11 shows the azimuthal mean error variances of the 10-m wind amplitude at different scales in ensembles integrated over the TC inherent region (a 300-km radius from the center) as a function of the lead time for PertD01, PertD02, and PertD03 of Typhoons Chan-hom and Maysak. The temporal mean variability of the 10-m wind amplitude of the Ctrl experiment in the same region (black dashed lines) is shown as a reference. The time points at which the error variance exceeds the reference are regarded as the predictability limit at that scale. It is noticeable that for both Typhoons Chan-hom and Maysak the mesoscale and convective scales (wave numbers ≥ 6) can only be predicted up to 6 h if the initial errors are superposed in the near (i.e., PertD02) or TC inner-core (i.e., PertD03) regions (see Fig. 11a2, 11a3, 11b2, and 11b3). If only the far environment is perturbed (i.e., PertD01), then the predictability limit of these scales can be slightly extended to 12–18 h (Fig. 11a1 and 11b1). In contrast with the conclusion of Judt et al. (2016) that the rainbands are predictable within a few days, we found that the rainband scales at wave numbers 3–5 can only be predicted within the first 18 h regardless of the regions of the initial errors. These different results possibly indicate that the initial uncertainties may degrade the prediction performance of the rainband-scale features more severely at earlier lead times than the model uncertainties. It could also mean that the two typhoon cases analyzed in this study have lower predictability than Hurricane Earl, which was the subject of the study in Judt et al. 2016. On the other hand, our results are consistent with the results of Judt et al. (2016) in that the mean flow of the TC (wave number 0; not shown) and the major asymmetrical components

(wave numbers 1–2) are resistant to the upscale error propagation from smaller scales and remain predictable for a much longer time of at least 3.5 days.

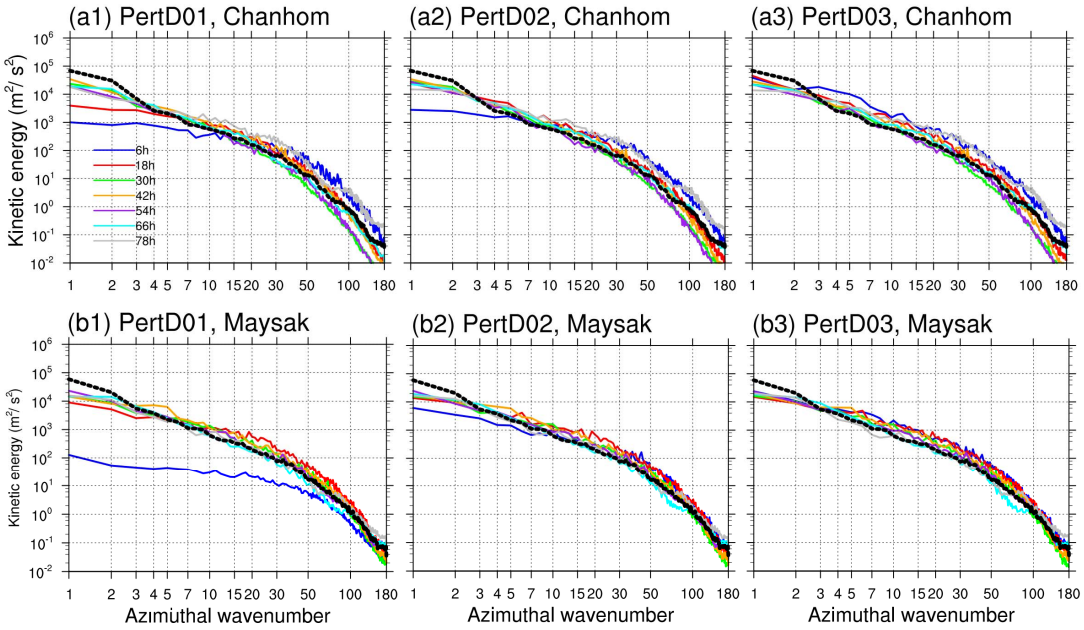

Figure 11. Azimuthally mean and regionally integrated (0–300 km) error variances (m^2 s^{-2}) at different scales of the 10-m wind amplitude averaged over all ensemble members at different lead times for (a1, b1) PertD01, (a2, b2) PertD02, and (a3, b3) PertD03 of (a) Typhoon Chan-hom and (b) Typhoon Maysak.

As shown in Fig. 11a2 and 11a3, the rainband scales of wave numbers 3–5 for Typhoon Chan-hom are still predictable at 6 h in PertD02 but are almost unpredictable at 6 h in PertD03. We therefore also show the 6-h composite radar reflectivity in D03, which roughly reflects the TC-induced rainfall in the Ctrl and ensemble forecasts of PertD02 and PertD03 (Fig. 12). Only three arbitrarily selected members are shown. Fig. 12a shows a clear spiral rainfall structure in the Ctrl experiment, extended from the south to the east and northeast of Typhoon Chan-hom, with most regions >30 dBZ. The southern rainfall conglomeration (highlighted with a purple rectangle in Fig. 12a) is organized as a cluster of convective storms and the eastern rainfall conglomeration (highlighted with a black rectangle in Fig. 12a) is characterized by a narrow, north–south stretched rainband. Noticeably, the members in PertD02 with initial perturbations in the near environment capture the placement and structure of the eastern rainband and the convective rainfall at 6 h (*cf.* shaded and black contours). However, the members in PertD03 with initial perturbations in the TC inner core present poor skill in predicting the long rainband in the east, with significant errors in both position and strength. In addition, the convective storms in the south of Typhoon Chan-hom in the ensembles of PertD03 are almost randomly distributed or completely displaced compared with those in the Ctrl experiment. The comparison indicates that the initial errors in the TC inner core can intensively constrain the predictability limit of the TC rainbands to <6 h.

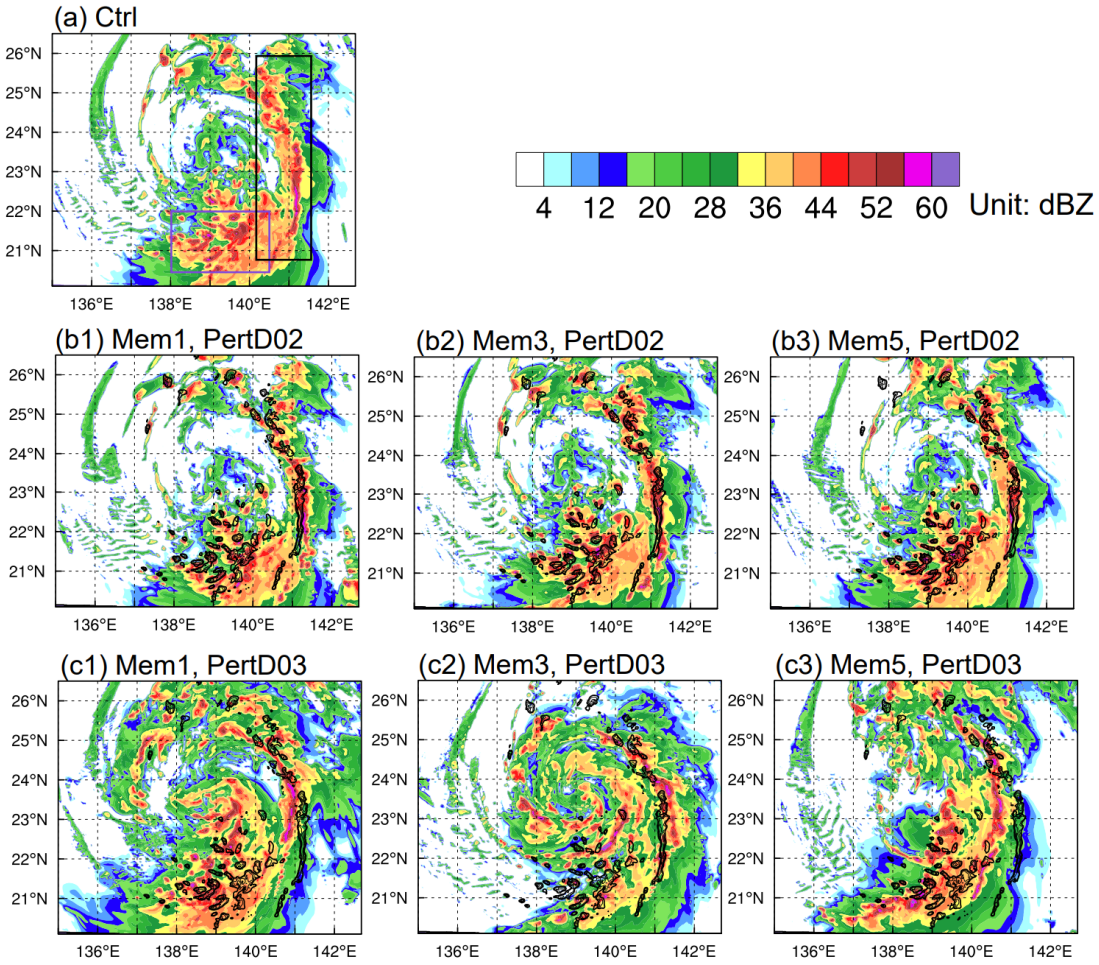

Figure 12. Composite radar reflectivity (shaded) in D03 of in the 6-h (a) Ctrl and (b1–b3) ensemble forecasts of PertD02 and (c1–c3) PertD03. The composite radar reflectivity (≥44 dBZ) of the Ctrl experiment is shown as black contours in (b1–b3) and (c1–c3) for comparison.

5.3 Source of predictability in the TC intensity

Fig. 11 shows that wave numbers 0–2 of the 10-m wind amplitude are resilient to the upscale error growth, in contrast with the fast growth and saturation of the errors at smaller scales. To understand the source of the predictability of the low wavenumber components, a supplementary experiment (hereafter called PertD03-RndD01) was carried out. This experiment was similar to PertD03 but additionally replaced the initial conditions of D01 in the ensemble forecasts with the variable fields downscaled from the GFS analysis at another valid time. In PertD03-RndD01, D01 for both Typhoons Chan-hom and Maysak uses the downscaled analysis at 0000 UTC on 18 August 2020, which is nearly two months and ten days, respectively, from the initial times of the experiment.

Fig. 13 shows the temporal evolution of the wave spectrum of the surface wind of the TC inner core for experiment PertD03-RndD01. Wave numbers ≥2 become saturated in <6 h, the same as in PertD03 (see Fig. 12). However, the error variances of wave numbers 1–2 become

nearly saturated within about one day, in contrast with those in PertD03 (see Fig. 12), which remain predictable at 3.5 days. This result indicates that the major source of the predictability of the surface wind components at wave numbers 1–2 is the synoptic-scale environment of the TC, which is consistent with the conclusions of Judt et al. (2016). The error variance of the mean vortex flow (i.e., wave number 0) is still significantly smaller than the saturation value, even with a nearly chaotic environmental field (not shown), implying that the TC mean vortex may be efficiently predicted for a fairly long time.

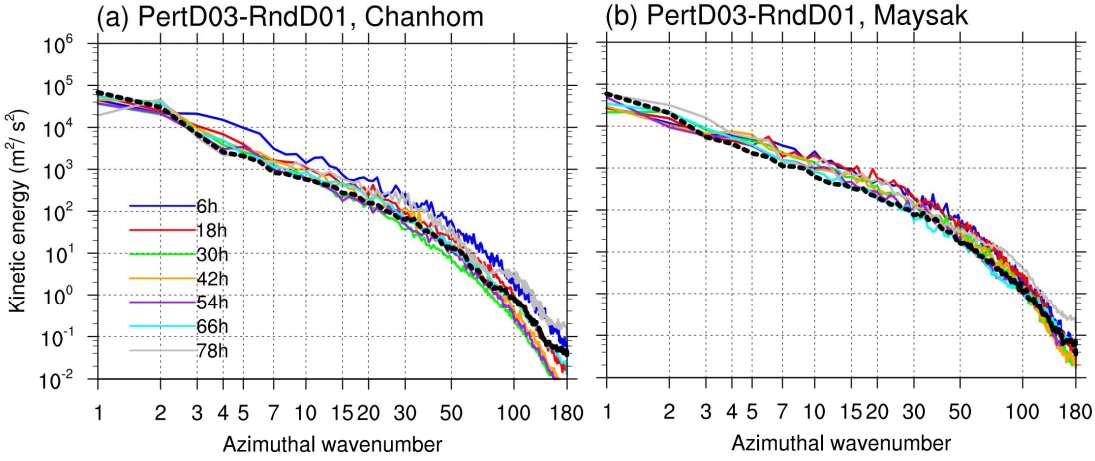

Figure 13. Same as Fig. 11 but for PertD03-RndD01 of (a) Typhoon Chan-hom and (b) Typhoon Maysak.

Fig. 14 shows the original 10-m wind speed field in the 300-km radius of the Ctrl experiment for Typhoon Chan-hom at 66 h and its composite wind field for wave numbers 0–2 (Fig. 14a and 14b). The composite surface wind of wave numbers 0–2 in the PertD03 and PertD03-RndD01 ensembles are also shown for comparison (Fig. 14c1–c5 and 14d1–d5, respectively). Wave components 0–2 can explain almost 95% of the variance of the 10-m wind amplitude in the Ctrl experiment (*cf*. Fig. 14a and 14b). When comparing the ensemble members of PertD03 and PertD03-RndD01, the formers can roughly capture the composite surface wind structure of wave numbers 0–2 in the Ctrl experiment (*cf*. shading and contours) with a mean spatial correlation of 0.94, which is much better than the latter of 0.83. This result is consistent with the lower error variance at wave numbers 0–2 in PertD03 than in PertD03-RndD01 (*cf*. Figs 11a3 and 13a).

Although the composite surface wind amplitude of waves 0–2 in PertD03 has a longer predictability limit than that in PertD03-RndD01 (at least 3.5 days versus almost one day), PertD03 shows a similar performance to PertD03-RndD01 in terms of the MSLP and MSW for both typhoons (*cf*. Fig. 9, cyan and purple curves), except for the MSLP of Typhoon Chan-hom. This suggests that the MSW has limitations as a metric to measure TC intensity (Vukicevic et al., 2014; Judt et al., 2016). The MSW defines the 10-m maximum wind speed at a certain time and point, which is not only related to wave numbers 0–2 but also has contribution from the highly turbulent, rapidly evolving asymmetrical wind field in TCs that has very low predictability.

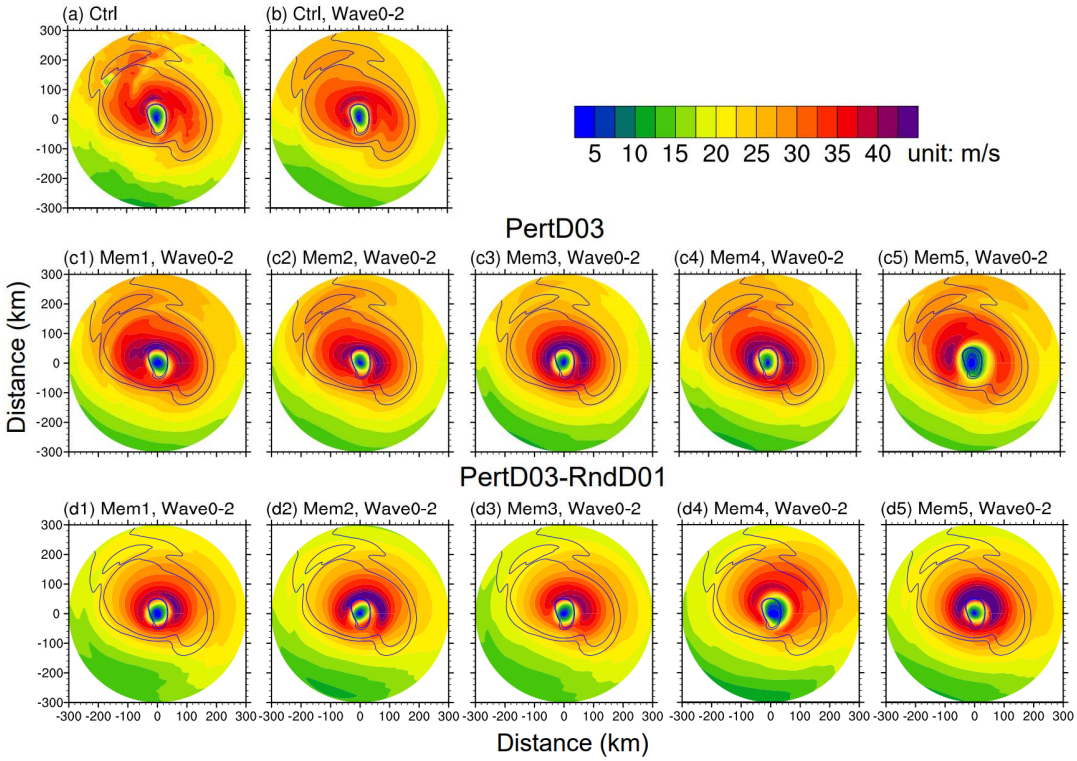

Figure 14. (a) 10-m wind speed forecast (shading) in the 300-km radius of the Ctrl experiment at 66 h for Typhoon Chan-hom and (b) its composite wind field (shading) of wave numbers 0–2. (c1–c5) Composite 10-m wind speed fields (shading) of wave numbers 0–2 of the ensemble forecasts for PertD03 at 66 h. (d1–d5) are same as (c1)-(c5) but for PertD03-RndD01 at 66 h. Blue contours highlight wind speeds of 25 and 27.5 m s^{-1} in the composite wind field of the Ctrl experiment in part (b).

6 Combined effects of initial and lateral boundary perturbations on the TC predictability

For practical predictions of TCs, uncertainties exist in not only the initial conditions but also the boundary conditions. This section considers the combined effects of the initial perturbations in all three nested domains and the boundary perturbations (i.e., PertALL) on the TC track and intensity predictability. Fig. 15 compares the ensemble-averaged errors in the TC track and intensity errors between PertALL and the worst-performing experiment (i.e., the largest forecast error) among PertD01, PertD02, and PertD03. These are PertD03 for the track and intensity of Typhoon Chan-hom and PertD01 for the track and PertD03 for the intensity of Typhoon Maysak (see Figs 4 and 9). The comparison in Fig. 15 shows that PertALL has larger forecast errors in both the track and intensity than the experiments with initial errors in particular regions for both Typhoons Chan-hom and Maysak. This means that the track and intensity of the TC become more unpredictable when taking into account all the sources of uncertainties in the initial and boundary conditions.

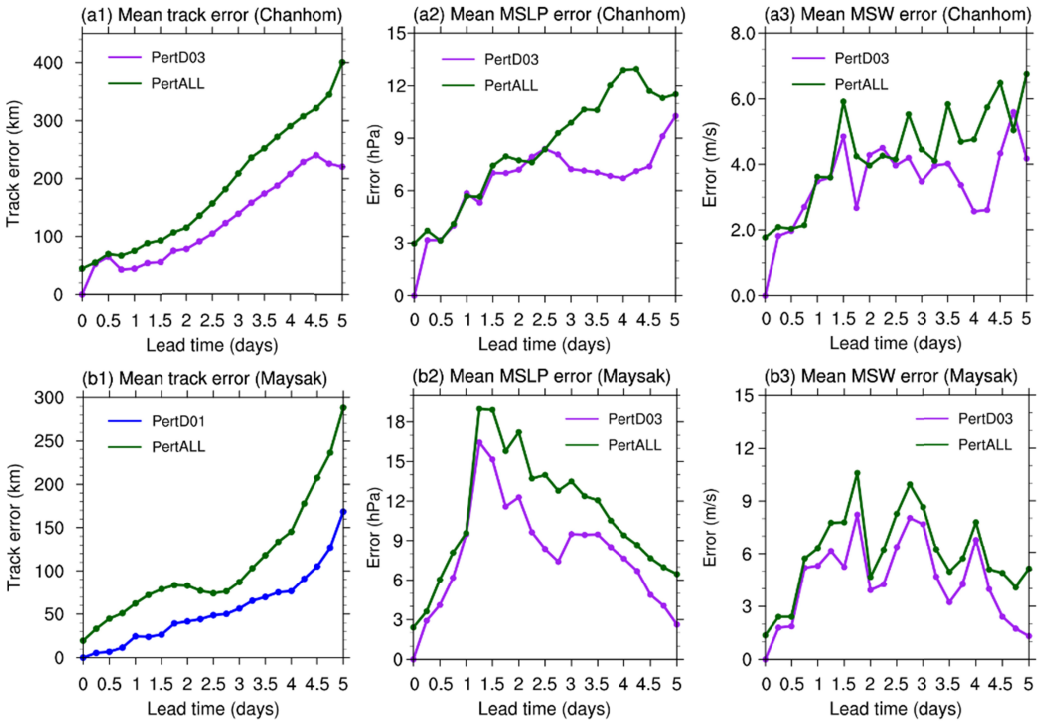

552

553 Figure 15. Ensemble-averaged forecast errors of the (a1, b1) track, (a2, b2) MSLP, and (a3, b3)
554 MSW for PertALL (dark green) and PertD03 (purple) of (a) Typhoon Chan-hom and (b)
555 Typhoon Maysak. In Fig. 15b1, PertALL is compared with PertD01 because the latter has the
556 worst performance in all other experiments.

557

558 Fig. 16 shows the ensemble-averaged error variance spectrum of the 10-m wind
559 amplitude in the TC inner core of PertALL. The temporal evolution of the error spectrum in
560 PertALL is similar to that in PertD03, although PertALL has larger forecast errors in the MSW
561 than PertD03 (see Fig. 15). The wind components of wave numbers 0–2 remain predictable for
562 about three days, which shows that the scales of wave numbers 0–2, which inherit their
563 predictability from the TC environment, are the major source that facilitates a skillful prediction
564 of TC intensity up to a few days.

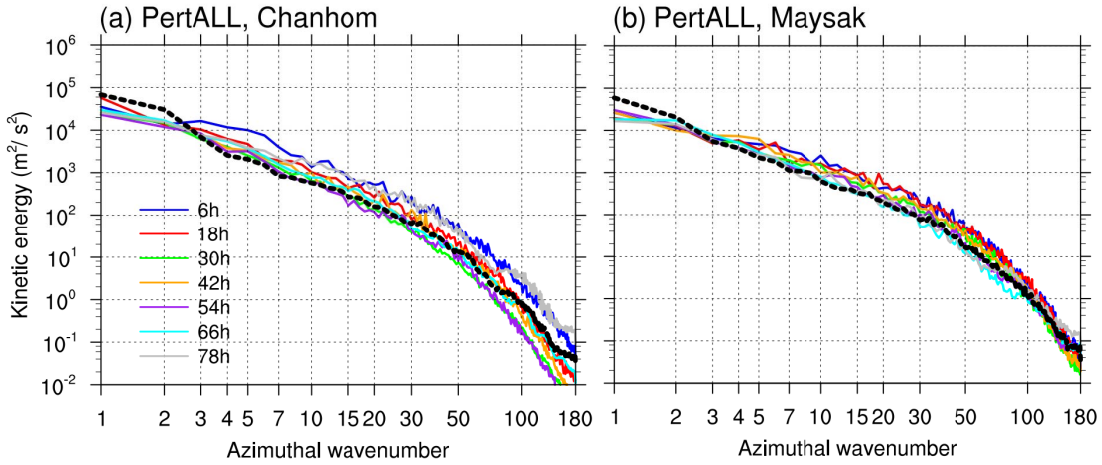

565

Figure 16. Same as Fig. 13 but for PertALL.

7 Conclusions and discussion

Gaining a profound comprehension of the intrinsic predictability of TCs is vital for enhancing the accuracy of their track and intensity forecasts. The concept of intrinsic predictability centers on how initial errors amplify and impact the prediction outcome when an almost perfect procedure is employed. This can offer a rough estimate of the upper limit of the predictive skill and the predictability threshold. To examine the intrinsic predictability of TC track and intensity, we compared convection-resolving control forecasts and ensemble forecasts with perturbed initial conditions using a regional HWRF model. Our primary objective was to investigate the sensitivity of TC track and intensity uncertainties to initial errors in various regions and the corresponding error growth dynamics. A model configuration with three two-way nested domains (18/6/2 km resolution) was used to provide a relatively realistic simulation of the scales and characteristics of the inner core and environment of TCs. Experiments were designed to investigate the influence of the initial errors in (1) the far environment (1300–3500 km from the TC center), (2) the near environment (350–1300 km), and (3) TC inner core and outer rainband regions (0–350 km) on the predictability of the track and intensity. We selected two typhoons, Chan-hom and Maysak, that occurred in the western North Pacific Ocean in 2020 and distinct uncertainty in both track and intensity to demonstrate the case-specific nature of predictability analysis. Our main results are summarized here.

(1) The most sensitive region of the initial errors that affect the TC track uncertainties is case-dependent. For a case with remarkably large track errors (e.g., Typhoon Chan-hom), the most sensitive region of the initial errors is the combined region of the TC inner core and outer rainbands (0–350 km). The strong interaction of the initial errors in the TC inner core and outer rainbands may lead to increased uncertainties in the TC environment that degrade the track forecast performance (Fig. 6). The track uncertainties with initial errors in the combined area of the TC inner core and outer rainbands are nearly double those with initial errors in either region (Fig. 4a).

(2) By contrast, for a case (e.g., Typhoon Maysak) with a much more predictable track, the most sensitive region of initial errors is the near environment (350–1300 km) in the early stages (about 2.5 days) and then the far environment (1300–3500 km; Fig. 4b) in the later stages. In this case, the growth of the initial errors in the environment is dominant in the track forecast as a result of the weak interactions between the TC inner and outer structures (Fig. 7).

(3) The most sensitive region of the initial errors for uncertainties in intensity is the inner core region (0–250 km) for both cases. Our results emphasize that not only the scale of the initial or model perturbations but also the regions of these perturbations, matter in the predictability of the TC intensity and track.

(4) Our results are consistent with the conclusions of Judt (2016) that the errors at meso- and convective scales (wave numbers ≥6) of the TC inner core grow rapidly and saturate within 6–12 h, regardless of the regions of the initial errors. However, we found the rainband scales at wave numbers 3–5 can only be predicted up to 18 h regardless of the regions of the initial errors, rather

than the few days of Judt (2016). This suggests the initial errors could possibly constrain the predictability of the features at the rainband scale more severely than the model errors.

(5) The mean vortex and asymmetrical structures of the TC at wave numbers 1–2 remain predictable for at least 3.5 days because their predictability source is the synoptic-scale environmental flow. Nevertheless, a more accurate environmental flow may not guarantee an improved prediction of the MSLP and MSW because these two instantaneous metrics are also influenced by highly turbulent and rapidly evolving finer-scale features that have very short predictability.

Although the influences of the region-dependent initial errors on uncertainties in the TC track and intensity were analyzed and compared and the most sensitive regions identified in this study, we still do not know the precise mechanisms of how the initial errors in different regions induce uncertainties in TC track and intensity. For Typhoon Chan-hom with significant track errors, how do the initial errors in the TC inner core and outer rainbands intensively interact and influence the TC environment and track? Why are the interactions between the inner and outer structures of Typhoon Maysak significantly weaker than those of Typhoon Chan-hom? Which physical processes in the TC inner core cause the remarkable intensity uncertainties of Typhoons Chan-hom and Maysak? These questions remain unclear and need further exploration in future studies.

Acknowledgments

The authors are grateful to Drs. Yuntao Wei and Guokun Dai at Fudan University, Dr. Deming Meng at Nanjing University, Prof. Tao Lian at the Second Institute of Oceanography, Profs. Wenjun Zhang, Xiefei Zhi, Qingqing Li, and Chao Wang at Nanjing University of Information Science and Technology in China for their input and helpful discussions. This study was supported by the National Natural Science Foundation of China (Grant No. 42288101 and 42105054).

Open Research

The global ensemble forecast product of GEFS at NCEP is downloaded from NCEP operational product inventory at https://www.nco.ncep.noaa.gov/pmb/products/gens/. The forecast product of the global forecast system (GFS) at NCEP is downloaded from https://rda.ucar.edu/datasets/ds084.1/. The Typhoon best-track data can be downloaded from the data archive center at https://ncics.org/ibtracs/index.php?name=YearBasin-2020

References

Anwender, D., Harr, P. A., and Jones, S. C. (2008). Predictability associated with the downstream impacts of the extratropical transition of tropical cyclones: Case studies. *Mon. Wea. Rev.*, *136*, 3226–3247, doi:10.1175/2008MWR2249.1.

Ashcroft, J., Schwendike, J., Griffiths, S. D., Ross, A. N., & Short, C. J. (2021). The impact of weak environmental steering flow on tropical cyclone track predictability. *Quarterly Journal of the Royal Meteorological Society, 147(741)*, 4122–4142. https://doi.org/10.1002/qj.4171

Black, M. L., Gamache, J. F., Marks, J. D., Samsury, C. E., & Willoughby, H. E. (2002). Eastern pacific Hurricanes Jimena of 1991 and Olivia of 1994: The effect of vertical shear on structure and intensity. *Monthly Weather Review, 130(9)*, 2291–2312. https://doi.org/10.1175/1520-0493(2002)130<2291:EPHJOA>2.0.CO;2

Cangialosi JP, Franklin JL. 2014. 'National Hurricane Center forecast verification report'. http://www.nhc.noaa.gov/verification/pdfs/ Verification_2013.pdf

Chen, S. S., Knaff, J. A., & Marks, F. D. (2006). Effects of vertical wind shear and storm motion on tropical cyclone rainfall asymmetries deduced from TRMM. *Monthly Weather Review, 134(11)*, 3190–3208. https://doi.org/10.1175/MWR3245.1

Chen, S. S., Price, J. F., Zhao, W., Donelan, M. A., & Walsh, E. J. (2007). The CBLAST-Hurricane program and the next-generation fully coupled atmosphere-wave-ocean models for hurricane research and prediction. *Bulletin of the American Meteorological Society, 88(3)*, 311–317. https://doi.org/10.1175/BAMS-88-3-311

Chen, S. S., Zhao, W., Donelan, M. A., & Tolman, H. L. (2013). Directional wind-wave coupling in fully coupled atmosphere-wave-ocean models: Results from CBLAST-hurricane. *Journal of the Atmospheric Sciences, 70(10)*, 3198–3215. https://doi.org/10.1175/JAS-D-12-0157.1

Chia, H. H., and Ropelewski, C. F. (2002). The interannual variability in the genesis location of tropical cyclones in the northwest Pacific. *Journal of Climate, 15(20)*, 2934–2944. https://doi.org/10.1175/1520-0442(2002)015<2934:TIVITG>2.0.CO;2

DeMaria, M., Sampson C. R., Knaff, J. A., and Musgrave, K. D., (2014). Is tropical cyclone intensity guidance improving? Bull. Amer. Meteor. Soc., *95*, 387–398, doi:10.1175/BAMS-D-12-00240.1.

Durran, D., and Gingrich M., (2014). Atmospheric predictability: Why butterflies are not of practical importance. *J. Atmos. Sci.*, *71*, 2476–2488, doi:10.1175/JAS-D-14-0007.1.

Emanuel, K. A. (1986). An air-sea interaction theory for tropical cyclones. Part I: steady-state maintenance. *Journal of the Atmospheric Sciences, 43(6)*, 585–604. https://doi.org/10.1175/1520-0469(1986)043<0585:aasitf>2.0.co;2

Emanuel, K., DesAutels, C., Holloway, C., & Korty, R. (2004). Environmental control of tropical cyclone intensity. *Journal of the Atmospheric Sciences, 61(7)*, 843–858. https://doi.org/10.1175/1520-0469(2004)061<0843:ECOTCI>2.0.CO;2

Feng, J. and Wang, X. G., (2019). Impact of assimilating upper-level dropsonde observations collected during the TCI field campaign on the prediction of intensity and structure of Hurricane Patricia (2015), *Mon. Wea. Rev., 147*, 3069–3089.

Feng, J. and Wang, X. G., (2021). Impact of increasing horizontal and vertical resolution of the hurricane WRF model on the analysis and prediction of Hurricane Patricia (2015). *Mon. Wea. Rev., 149(2)*, 419–441. DOI: 10.1175/MWR-D-20-0144.1

Feng, J., Qin, X., Wu, C., Zhang, P., Yang, L., Shen, X. S., Han, W., Liu, Y. Z., (2022) Improving typhoon predictions by assimilating the retrieval of atmospheric temperature profiles from the FengYun-4A's Geostationary Interferometric Infrared Sounder (GIIRS), *Atmospheric Research, 280*, 106391, ISSN 0169-8095, https://doi.org/10.1016/j.atmosres.2022.106391.

Ferrier, B. S., (1994). A double-moment multiple-phase four-class bulk ice scheme. Part I: Description. *J. Atmos. Sci.*, *51*, 249–280, https://doi.org/10.1175/1520-0469(1994)051<0249:ADMMPF>2.0.CO;2.

Ferrier, B. S., (2005). An efficient mixed-phase cloud and precipitation scheme for use in operational NWP models. *2005 Spring Meeting,* San Francisco, CA, Amer. Geophys. Union, Abstract A42A-02.

Finocchio, P. M., & Majumdar, S. J. (2017). The Predictability of Idealized Tropical Cyclones in Environments With Time-Varying Vertical Wind Shear. *Journal of Advances in Modeling Earth Systems, 9(8)*, 2836–2862. https://doi.org/10.1002/2017MS001168

Gopalakrishnan, S. G., Marks, F., Zhang, X., Bao, J. W., Yeh, K. S., & Atlas, R. (2011). The experimental HWRF system: A study on the influence of horizontal resolution on the structure and intensity changes in tropical cyclones using an idealized framework. *Monthly Weather Review, 139(6)*, 1762–1784. https://doi.org/10.1175/2010MWR3535.1

Hakim, G. J. (2013). The variability and predictability of axisymmetric hurricanes in statistical equilibrium. *Journal of the Atmospheric Sciences, 70(4)*, 993–1005. https://doi.org/10.1175/JAS-D-12-0188.1

Han, J., and Pan, H.-L., (2006). Sensitivity of hurricane intensity forecasts to convective momentum transport parameterization. *Mon. Wea. Rev.*, *134*, 664–674, https://doi.org/10.1175/MWR3090.1.

Hong, S.-Y., and Pan, H.-L., (1996). Nonlocal boundary layer vertical diffusion in a medium-range forecast model. *Mon. Wea. Rev.*, *124*, 2322–2339, https://doi.org/10.1175/15200493(1996)124<2322:NBLVDI>2.0.CO;2.

Houze, R. A. (2010, February). Clouds in tropical cyclones. Monthly Weather Review. https://doi.org/10.1175/2009MWR2989.1

Harr, P. A., Anwender, D., and Jones, S. C., (2008). Predictability associated with the downstream impacts of the extratropical transition of tropical cyclones: Methodology and a case study of Typhoon Nabi (2005). *Mon. Wea. Rev.*, *136*, 3205–3225, doi:10.1175/2008MWR2248.1.

Hazelton, A., Alaka Jr, G. J., Fischer, M. S., Torn, R., & Gopalakrishnan, S. (2023). Factors Influencing the Track of Hurricane Dorian (2019) in the West Atlantic: Analysis of a HAFS Ensemble. *Monthly Weather Review, 151(1)*, 175–192

Holland, G. J. (Ed.) (1993), Tropical cyclone motion, in Global Guide to Tropical Cyclone Forecasting, Tech. Doc. WMO/TD 560, Trop. Cyclone Programme Rep. TCP-31, chap. 3, World Meteorol. Org., Geneva, Switzerland. (Available at http://www.bom.gov.au/bmrc/pubs/tcguide/ch3/ch3_tableo

Houze, R. A., Chen, S. S., Lee, W.-C., Rogers, R. F., Moore, J. A., Stossmeister, G. J., … Brodzik, S. R. (2006). The Hurricane Rainband and Intensity Change Experiment: Observations and Modeling of Hurricanes Katrina, Ophelia, and Rita. *Bulletin of the American Meteorological Society, 87(11)*, 1503–1522. https://doi.org/10.1175/bams-87-11-1503

Ito, K., & Wu, C. C. (2013). Typhoon-position-oriented sensitivity analysis. part I: Theory and verification. *Journal of the Atmospheric Sciences, 70(8)*, 2525–2546. https://doi.org/10.1175/JAS-D-12-0301.1

Judt, F., and S. S. Chen, 2010: Convectively generated potential vorticity in rainbands and formation of the secondary eyewall in Hurricane Rita of 2005. *J. Atmos. Sci.*, *67*, 3581–3599.

Judt, F., & Chen, S. S. (2016). Predictability and dynamics of tropical cyclone rapid intensification deduced from high-resolution stochastic ensembles. *Monthly Weather Review, 144(11)*, 4395–4420. https://doi.org/10.1175/MWR-D-15-0413.1

Judt, F., Chen, S. S., & Berner, J. (2016). Predictability of tropical cyclone intensity: Scale-dependent forecast error growth in high-resolution stochastic kinetic-energy backscatter ensembles. *Quarterly Journal of the Royal Meteorological Society, 142(694)*, 43–57. https://doi.org/10.1002/qj.2626

Katz, R. W., and Murphy, A. H., (2015). *Economic Value of Weather and Climate Forecasts*. Cambridge University Press, 240 pp.

Kieu, C. Q., and Moon, Z. (2016). Hurricane intensity predictability. *Bulletin of the American Meteorological Society, 97(10)*, 1847–1857. https://doi.org/10.1175/BAMS-D-15-00168.1

780 Kieu, C. and Rotunno, R. (2022). Characteristics of Tropical-Cyclone Turbulence and Intensity
781 Predictability. *Geophysical Research Letters*, *49*(8). https://doi.org/10.1029/2021GL096544
782
783 Kwon, Y. C., Lord, S., Lapenta, B., Tallapragada, V., Liu, Q., and Zhang, Z., (2010). Sensitivity
784 of air-sea exchange coefficients (Cd and Ch) on hurricane intensity. *29th Conf. on Hurricanes*
785 *and Tropical Meteorology,* Tucson, AZ, Amer. Meteor. Soc.,
786 13C.1, https://ams.confex.com/ams/29Hurricanes/techprogram/paper_167760.htm.
787
788 Lacis, A. A., and Hansen, J. E., (1974). A parameterization for the absorption of solar radiation
789 in the earth's atmosphere. *J. Atmos. Sci.*, *31*, 118–133, https://doi.org/10.1175/1520-
790 0469(1974)031<0118:APFTAO>2.0.CO;2.
791
792 Li, Q., & Wang, Y. (2012). A comparison of inner and outer spiral rainbands in a numerically
793 simulated tropical cyclone. *Monthly Weather Review, 140(9)*, 2782–2805.
794 https://doi.org/10.1175/MWR-D-11-00237.1
795
796 Lorenz, E. N., (1969). The predictability of a flow which possesses many scales of
797 motion. *Tellus*, *21*, 289–307, https://doi.org/10.3402/tellusa.v21i3.10086.
798
799 Lorenz, E. N., (1996). Predictability—A problem partly solved. *Proc. Seminar on*
800 *Predictability*, Reading, United Kingdom, ECMWF, 1–18.
801 Lu, X., Wang, X., Tong, M., & Tallapragada, V. (2017). GSI-based, continuously cycled, dual-
802 resolution hybrid ensemble-variational data assimilation system for HWRF: System description
803 and experiments with edouard (2014). *Monthly Weather Review, 145(12)*, 4877–4898.
804 https://doi.org/10.1175/MWR-D-17-0068.1
805
806 Ma, Z., Fei, J., Liu, L., Huang, X., & Li, Y. (2017). An investigation of the influences of
807 mesoscale ocean eddies on tropical cyclone intensities. *Monthly Weather Review, 145(4)*, 1181–
808 1201. https://doi.org/10.1175/MWR-D-16-0253.1
809
810 Ma, Z., Fei, J., Huang, X., & Cheng, X. (2018). Modulating Effects of Mesoscale Oceanic
811 Eddies on Sea Surface Temperature Response to Tropical Cyclones Over the Western North
812 Pacific. *Journal of Geophysical Research: Atmospheres, 123(1)*, 367–379.
813 https://doi.org/10.1002/2017JD027806
814
815 Moeng, C. H., Dudhia, J., Klemp, J., & Sullivan, P. (2007). Examining two-way grid nesting for
816 large eddy simulation of the PBL using the WRF model. *Monthly Weather Review, 135(6)*,
817 2295–2311. https://doi.org/10.1175/MWR3406.1
818
819 Moller, J. D., & Montgomery, M. T. (2000). Tropical cyclone evolution via potential vorticity
820 anomalies in a three-dimensional balance model. *Journal of the Atmospheric Sciences, 57(20)*,
821 3366–3387. https://doi.org/10.1175/1520-0469(2000)057<3366:TCEVPV>2.0.CO;2
822
823 Nystrom, R. G., Zhang, F., Munsell, E. B., Braun, S. A., Sippel, J. A., Weng, Y., & Emanuel, K.
824 (2018). Predictability and dynamics of Hurricane Joaquin (2015) explored through convection-

permitting ensemble sensitivity experiments. *Journal of the Atmospheric Sciences, 75(2)*, 401–424. https://doi.org/10.1175/JAS-D-17-0137.1

Nolan, D. S., Moon, Y., & Stern, D. P. (2007). Tropical cyclone intensification from asymmetric convection: Energetics and efficiency. *Journal of the Atmospheric Sciences, 64(10)*, 3377–3405. https://doi.org/10.1175/JAS3988.1

Persing, J., Montgomery, M. T., McWilliams, J. C., & Smith, R. K. (2013). Asymmetric and axisymmetric dynamics of tropical cyclones. *Atmospheric Chemistry and Physics, 13(24)*, 12299–12341. https://doi.org/10.5194/acp-13-12299-2013

Qin, N., Wu, L., & Liu, Q. (2021). Evolution of the moat associated with the secondary eyewall formation in a simulated tropical cyclone. *Journal of the Atmospheric Sciences, 78(12)*, 4021–4035. https://doi.org/10.1175/JAS-D-20-0375.1

Qin, N., Wu, L., Liu, Q., and Zhou, X., (2023). Driving forces of extreme updrafts associated with convective bursts in the eyewall of a simulated tropical cyclone. *Journal of Geophysical Research: Atmospheres (J. Geophys. Res.), 128*, e2022JD037061. https://doi.org/10.1029/2022JD037061

Rios-Berrios, R., and R. D. Torn, 2017: Climatological analysis of tropical cyclone intensity changes under moderate vertical wind shear. *Mon. Wea. Rev.*, *145*, 1717–1738, https://doi.org/10.1175/MWR-D-16-0350.1.

Rogers, R. (2010). Convective-scale structure and evolution during a high-resolution simulation of tropical cyclone rapid intensification. *Journal of the Atmospheric Sciences, 67(1)*, 44–70. https://doi.org/10.1175/2009JAS3122.1

Schwarzkopf, M. D., and Fels, S., (1991). The simplified exchange method revisited: An accurate, rapid method for computation of infrared cooling rates and fluxes. *J. Geophys. Res.*, *96*, 9075–9096, https://doi.org/10.1029/89JD01598.

Selz, T. (2019). Estimating the intrinsic limit of predictability using a stochastic convection scheme. *Journal of the Atmospheric Sciences, 76(3)*, 757–765. https://doi.org/10.1175/JAS-D-17-0373.1

Shapiro, L. J., & Willoughby, H. E. (1982). The response of balanced hurricanes to local sources of heat and momentum. *Journal of the Atmospheric Sciences, 39(2)*, 378–394. https://doi.org/10.1175/1520-0469(1982)039<0378:TROBHT>2.0.CO;2

Shin, S., & Smith, R. K. (2008). Tropical-cyclone intensification and predictability in a minimal three-dimensional model. *Quarterly Journal of the Royal Meteorological Society, 134(636)*, 1661–1671. https://doi.org/10.1002/qj.327

Sippel, J. A., & Zhang, F. (2008). A probabilistic analysis of the dynamics and predictability of tropical cyclogenesis. *Journal of the Atmospheric Sciences, 65(11)*, 3440–3459. https://doi.org/10.1175/2008JAS2597.1

Sippel, J. A., & Zhang, F. (2010). Factors affecting the predictability of Hurricane Humberto (2007). *Journal of the Atmospheric Sciences, 67(6)*, 1759–1778. https://doi.org/10.1175/2010JAS3172.1

Sun, Y. Q., & Zhang, F. (2016). Intrinsic versus practical limits of atmospheric predictability and the significance of the butterfly effect. *Journal of the Atmospheric Sciences, 73(3)*, 1419–1438. https://doi.org/10.1175/JAS-D-15-0142.1

Tang, B., & Emanuel, K. (2012). Sensitivity of tropical cyclone intensity to ventilation in an axisymmetric model. *Journal of the Atmospheric Sciences, 69(8)*, 2394–2413. https://doi.org/10.1175/JAS-D-11-0232.1

Tao, D., & Zhang, F. (2015). Effects of vertical wind shear on the predictability of tropical cyclones: Practical versus intrinsic limit. *Journal of Advances in Modeling Earth Systems, 7(4)*, 1534–1553. https://doi.org/10.1002/2015MS000474

Torn, R. D., Whitaker, J. S., Pegion, P., Hamill, T. M., & Hakim, G. J. (2015). Diagnosis of the source of GFS medium-range track errors in Hurricane Sandy (2012). *Monthly Weather Review, 143(1)*, 132–152. https://doi.org/10.1175/MWR-D-14-00086.1

Torn, R. D., Elless, T. J., Papin, P. P., & Davis, C. A. (2018). Tropical cyclone track sensitivity in deformation steering flow. *Monthly Weather Review, 146(10)*, 3183–3201. https://doi.org/10.1175/MWR-D-18-0153.1

Van Sang, N., Smith, R. K., & Montgomery, M. T. (2008). Tropical-cyclone intensification and predictability in three dimensions. *Quarterly Journal of the Royal Meteorological Society, 134(632)*, 563–582. https://doi.org/10.1002/qj.235

Wang, Y., & Wu, C. C. (2004, December). Current understanding of tropical cyclone structure and intensity changes - A review. *Meteorology and Atmospheric Physics.* https://doi.org/10.1007/s00703-003-0055-6

Wu, L., Wang, B., & Geng, S. (2005). Growing typhoon influence on east Asia. *Geophysical Research Letters, 32(18)*, 1–4. https://doi.org/10.1029/2005GL022937

Wu, T. C., Liu, H., Majumdar, S. J., Velden, C. S., & Anderson, J. L. (2014). Influence of assimilating satellite-derived atmospheric motion vector observations on numerical analyses and forecasts of tropical cyclone track and intensity. *Monthly Weather Review, 142(1)*, 49–71. https://doi.org/10.1175/MWR-D-13-00023.1

Yang, B., Wang, Y., & Wang, B. (2007). The effect of internally generated inner-core asymmetries on tropical cyclone potential intensity. *Journal of the Atmospheric Sciences, 64(4)*, 1165–1188. https://doi.org/10.1175/JAS3971.1

Zhang, B., Lindzen, R. S., Tallapragada, V., Weng, F., Liu, Q., Sippel, J. A., … Bender, M. A. (2016). Increasing vertical resolution in US models to improve track forecasts of Hurricane Joaquin with HWRF as an example. *Proceedings of the National Academy of Sciences of the United States of America, 113(42)*, 11765–11769. https://doi.org/10.1073/pnas.1613800113

Zhang, D. L., & Chen, H. (2012). Importance of the upper-level warm core in the rapid intensification of a tropical cyclone. *Geophysical Research Letters, 39(2)*. https://doi.org/10.1029/2011GL050578

Zhang, F., & Tao, D. (2013). Effects of vertical wind shear on the predictability of tropical cyclones. *Journal of the Atmospheric Sciences, 70(3)*, 975–983. https://doi.org/10.1175/JAS-D-12-0133.1

Zhang, S., Pu, Z., & Velden, C. (2018). Impact of enhanced atmospheric motion vectors on HWRF Hurricane analyses and forecasts with different data assimilation configurations. *Monthly Weather Review, 146(5)*, 1549–1569. https://doi.org/10.1175/MWR-D-17-0136.1

Zhong, Q., Li, J., Zhang, L., Ding, R., & Li, B. (2018). Predictability of tropical cyclone intensity over the Western North Pacific using the IBTrACS dataset. *Monthly Weather Review, 146(9)*, 2741–2755. https://doi.org/10.1175/MWR-D-17-0301.1

Zhou, X., Zhu, Y., Hou, D., Fu, B., Li, W., Guan, H., … Pegion, P. (2022). The Development of the NCEP Global Ensemble Forecast System Version 12. *Weather and Forecasting, 37(6)*, 1069–1084. https://doi.org/10.1175/waf-d-21-0112.1